

Fragment properties of fragmenting heavy nuclei produced in central and semi-peripheral collisions.

E. Bonnet ^{a,b}, B. Borderie ^{a,*}, N. Le Neindre ^{a,1}, M. F. Rivet ^a,
 R. Bougault ^c, A. Chbihi ^b, R. Dayras ^d, J. D. Frankland ^b,
 E. Galichet ^{a,e}, F. Gagnon-Moisan ^{a,f}, D. Guinet ^g, P. Lantesse ^g,
 J. Łukasik ^h, D. Mercier ^{c,g}, M. Pârlog ^{c,k}, E. Rosato ⁱ, R. Roy ^f,
 C. Sffienti ^j, M. Vigilante ⁱ, J. P. Wieleczko ^b and B. Zwieglinski ^ℓ

INDRA and ALADIN Collaborations

^a*Institut de Physique Nucléaire, CNRS/IN2P3, Université Paris-Sud 11, F-91406 Orsay cedex, France.*

^b*GANIL, CEA/DSM-CNRS/IN2P3, B.P. 5027, F-14076 Caen cedex, France.*

^c*LPC, CNRS/IN2P3, ENSICAEN, Université de Caen, F-14050 Caen cedex, France.*

^d*IRFU/SPhN, CEA Saclay, F-91191 Gif sur Yvette cedex, France.*

^e*Conservatoire National des Arts et Métiers, F-75141 Paris cedex 03, France.*

^f*Laboratoire de Physique Nucléaire, Département de Physique, de Génie Physique et d'Optique, Université Laval, Québec, Canada G1K 7P4.*

^g*Institut de Physique Nucléaire, CNRS/IN2P3, Université Claude Bernard Lyon 1, F-69622 Villeurbanne cedex, France.*

^h*Institute of Nuclear Physics IFJ-PAN, PL-31342 Kraków, Poland.*

ⁱ*Dipartimento di Scienze Fisiche e Sezione INFN, Università di Napoli "Federico II", I80126 Napoli, Italy.*

^j*Gesellschaft für Schwerionenforschung mbH, D-64291 Darmstadt, Germany.*

^k*National Institute for Physics and Nuclear Engineering, RO-76900 Bucharest-Măgurele, Romania.*

^ℓ*The Andrzej Soltan Institute for Nuclear Studies, PL-00681, Warsaw, Poland.*

Abstract

Fragment properties of hot fragmenting sources of similar sizes produced in central and semi-peripheral collisions are compared in the excitation energy range 5-10 A MeV. For semi-peripheral collisions a method for selecting compact quasi-projectiles sources in velocity space similar to those of fused systems (central colli-

sions) is proposed. The two major results are related to collective energy. The weak radial collective energy observed for quasi-projectile sources is shown to originate from thermal pressure only. The larger fragment multiplicity observed for fused systems and their more symmetric fragmentation are related to the extra radial collective energy due to expansion following a compression phase during central collisions. A first attempt to locate where the different sources break in the phase diagram is proposed.

Key words: Intermediate energy heavy-ion reactions, central and semi-peripheral collisions, multifragmentation, fragment partitions, collective energy

PACS: 25.70.-z, 25.70.Pq, 24.10.-i

1 Introduction

Heavy-ion collisions at intermediate energies offer various possibilities to produce hot nuclei which undergo a break-up into smaller pieces, which is called multifragmentation. This phenomenon is expected to bring information and constraints on the phase diagram of nuclear matter through measured fragment properties [1]. In particular by comparing in detail the properties of fragments emitted by hot nuclei formed in central and semi-peripheral collisions (i.e. with different dynamical conditions for their formation) one can expect to reveal features which characterize where those hot nuclei break in the phase diagram [2,3,4,5]. It is the final goal of this article; the first question being: do we see any different features in fragment properties ? For reactions at small impact parameters in the Fermi energy domain, one can select the collisions where the two nuclei merge into a quasi-fused system (QF) after full stopping [6]. At larger impact parameters and for higher incident energies, only a fraction of each nucleus interacts producing in the outgoing channel quasi-target (QT) and quasi-projectile (QP) sources. For both cases large energy dissipations occur but some constraints applied to nuclei are different with a compression-expansion cycle for central collisions and a friction-abrasion process which can produce dynamical emissions in the contact region (mid rapidity emissions) for peripheral collisions [7,8,9,10]. Therefore, to make a meaningful comparison of fragment properties which can be related to the phase diagram, hot nuclei showing to a certain extent statistical emission features must be selected. It is done for central collisions by selecting compact

* Corresponding author - [borderie@ipno.in2p3.fr](mailto:bonnet@ipno.in2p3.fr)
Email address: bonnet@ganil.fr (E. Bonnet).

¹ Present address: LPC Caen, ENSICAEN, Université de Caen, CNRS/IN2P3, F-14050 Caen Cedex, France

events in velocity space (flow angle selection). For peripheral collisions a selection method is proposed and applied to quasi-projectiles. Hot nuclei with A around 150-200 were produced at GANIL in $^{129}\text{Xe} + ^{\text{nat}}\text{Sn}$ central collisions at five bombarding energies in the range 25-50 A MeV and at GSI in semi-peripheral Au+Au collisions at 80 A MeV incident energy.

The paper is organized as follows. In section 2 we briefly present the experimental set-up and conditions. We recall the criteria allowing to select experimental events corresponding to fused systems. Then the method employed to extract the excited QPs is described. Global properties of the different selected sources are finally discussed using the excitation energy as control parameter. A comparison of fragment charge partitions associated with the different sources is shown in section 3. Section 4 presents a detailed study of kinetic fragment properties produced in central and peripheral collisions. Radial collective energies are compared by means of fragment relative velocities. Section 5 is devoted to discussion and conclusions.

2 Experimental selection

2.1 Experimental procedure

Beams of ^{129}Xe , accelerated at five incident energies: 25, 32, 39, 45 and 50 A MeV by the GANIL facility, bombarded a thin target of natural tin ($350 \mu\text{g}/\text{cm}^2$). Hot nuclei with A around 150-200 were produced in central collisions. Nuclei of similar masses were obtained at GSI in semi-peripheral Au+Au collisions at 80 A MeV incident energy. This energy appears to be a good compromise between high energy detection limit for H isotopes introduced by the detectors, a grazing angle within the measured angular range and a good characterization for QPs which are well separated from QTs in velocity space. For this experiment the ^{197}Au beam was impinging on a $2 \text{ mg}/\text{cm}^2$ ^{197}Au thick target.

The data were collected with the 4π multidetector INDRA which is described in detail in [11,12]. INDRA consists of 336 telescopes covering about 90% of the 4π solid angle. The configuration used at GSI differed in the composition of the first ring (2° - 3°): the phoswich scintillators were replaced by 12 telescopes, each composed of a $300 \mu\text{m}$ Si detector followed by a 14 cm long CsI(Tl) scintillator. Accurate fragment identification and energy calibration were achieved with INDRA; the energy of the detected products is obtained with an accuracy of 4%. Further details can be found in [13,14,15,16].

2.2 Event selection for quasi-fused systems

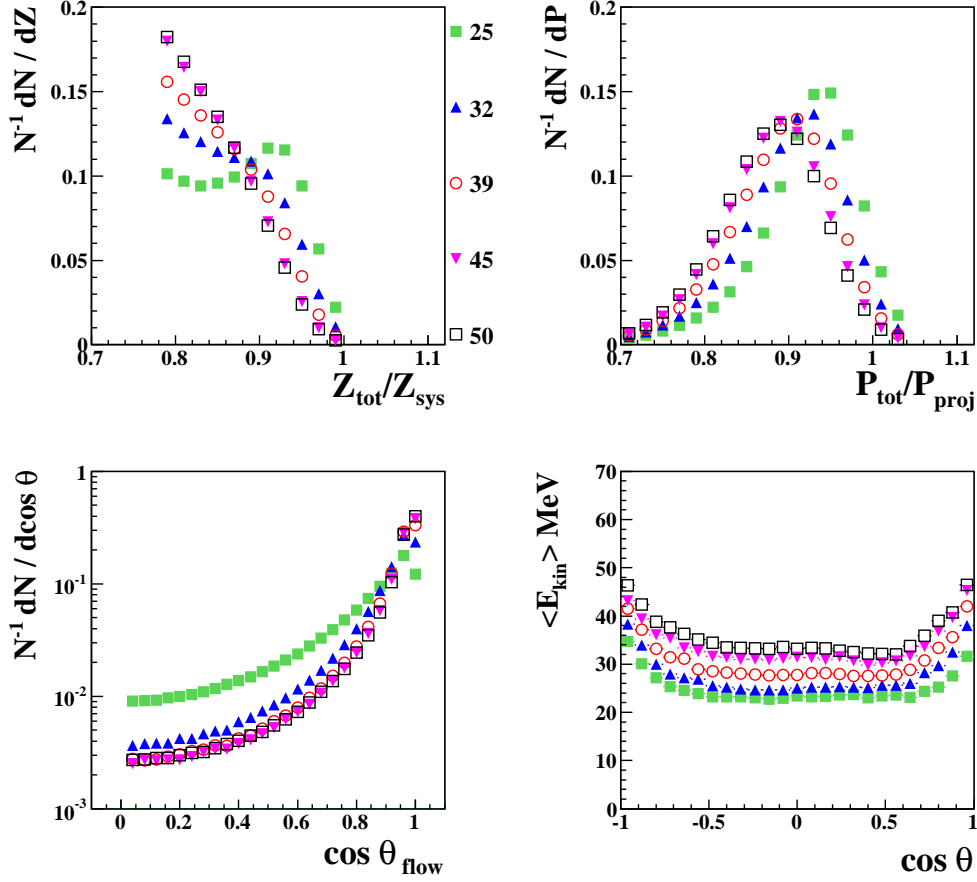


Fig. 1. Results for Xe+Sn central collisions at 5 energies: 25, 32, 39, 45 and 50 AMeV. Top - Normalized detected charge (left) and pseudo linear momentum (right) distributions of complete events. Bottom left panel: normalized angular distributions of the CM flow angle, for complete events; bottom right panel: mean kinetic energy vs c.m. angle for light charged particles ($Z \leq 4$) for the compact events ($\cos\theta_{flow} \leq 0.5$).

A two step procedure was used to select QF sources. First of all “complete experimental events” were selected by requiring that at least 80% of the total charge of the system was measured; the corresponding event distributions are displayed in the left upper part of fig. 1. That minimum percentage of the total charge induces a lower limit on the total pseudo linear momentum (P_{tot} / P_{proj} - see eq. 1) around 70% of the entrance channel value (see right upper part of fig. 1) and selects central collisions only.

$$P_{tot} = \left| \sum_{i=1}^{M_{tot}} \vec{\beta}_i \gamma_i Z_i \right| \quad (1)$$

M_{tot} is the total measured charged product multiplicity in the event. Then, compact single sources in velocity space were selected by imposing the constraint of flow angle $\geq 60^\circ$ [17,18,19]. To calculate θ_{flow} the kinetic energy tensor was built with fragments ($Z \geq 5$) and starting from fragment multiplicity $M_{frag} \geq 1$. Indeed it was shown in previous studies that while events present the topology of emission from two sources at small flow angles, they evolve towards a single-source configuration above 60° (see figure 9 in ref [18] and figure 1 in ref [6]). The rather flat $\cos \theta_{flow}$ distribution (variation of about 35% between $\theta_{flow}=60^\circ$ and 90°) observed for each incident energy in the selected range (see left bottom part of fig. 1) indicates a fragment emission which can be associated with a strong degree of equilibration. Note that such QF sources are produced at high excitation energy (above 3.0-3.5 A MeV) and their deexcitation through fission is suppressed [4].

The charged particles ($Z = 1-4$) to be associated with the single sources were determined from angular and energetic criteria. Figure 1 (right bottom part) shows the centre of mass average energy of particles in coincidence with the single sources as a function of their centre of mass emission angles. Large energies are measured forward-backward indicating preequilibrium emissions whereas rather constant average values are observed over a 2π solid angle (angular range $60^\circ-120^\circ$). So, assuming isotropic emission, twice the charged particles on that angular range were associated with the sources event by event [19].

Finally the calorimetric method [20] was used to evaluate the source excitation energy. The following hypotheses have been made: a level density parameter equal to $A/10$, the average kinetic energy of neutrons equal to their emitting source temperature and the Evaporation Attractor Line formula ($A=Z(2.072+2.32 \times 10^{-3}Z)$) [21] applied for fragment mass determinations. EAL is especially well adapted when heavy fragments ($Z > 20$) result from the deexcitation of the neutron deficient sources produced. More details on calorimetry are presented in the appendix. For all incident energies Gaussian distributions are obtained for the excitation energies of the source.

2.3 Selection of quasi-projectile sources

For peripheral collisions at 80 A MeV incident energy, the relativistic fragment ($Z \geq 5$) kinetic energy tensor (events with at least one fragment, $M_{frag} \geq 1$ - eq. 2) was computed in the centre of mass of the reaction to define the ellipsoid frame of each event, comprising M_{frag}^{tot} fragments.

$$T^{uv} = \sum_{i=1}^{M_{frag}^{tot}} \left(\sum_{u,v=1,3} \frac{P_i^{(u)} P_i^{(v)}}{(1 + \gamma_i) m_i} \right) \quad (2)$$

QP sources were selected through a completeness criterion on the total detected charge (eq. 3) and pseudo-momentum (eq. 4) on the forward part of each event - defined as all reaction products with a positive rapidity, M_{fwd} , in the ellipsoid frame.

$$Z_{fwd} = \sum_{i=1}^{M_{fwd}} Z_i \quad Z_{fwd}/Z_{proj} \in [0.80, 1.10] \quad (3)$$

$$P_{fwd} = \left| \sum_{i=1}^{M_{fwd}} \vec{\beta}_i \gamma_i Z_i \right| \quad P_{fwd}/P_{proj} \in [0.60, 1.10] \quad (4)$$

Z_{proj} and P_{proj} refer to projectile charge and momentum in the laboratory.

These preliminary selections lead to an ensemble of sub-events called complete QP events. Then the velocity of each reconstructed QP source is determined using fragments only.

To perform a meaningful comparison between the fragment properties of single sources defined in the previous section and QP sources, we must minimize the contribution of dynamical emissions for fragments. Indeed, in this energy regime and for peripheral and mid-peripheral collisions it is well known that a large part of the collisions end-up in two remnants coming from projectile and target and some particles and fragments with velocities intermediate between those of the remnants. They are called mid-rapidity products. They may have several origins: direct preequilibrium emission from the overlap region between the incident partners or a neck of matter between them which may finally separate from QP or QT, or from both, as well as emissions from QP/QT partially deformed and locally highly excited [9,10,22,23,24]. On the other hand, with higher dissipation associated with the decrease of the impact parameter, the velocities of the outgoing partners (QPs and QTs) are much closer to the centre of mass velocity, which makes difficult the definition of QP and QT sources. Therefore a compactness criterion in velocity space was defined and applied to select compact QP events among complete QP events which comprise at least two fragments. With this aim, we investigate further the global energetic properties of fragments. We define the VarDyn observable as follows:

$$\text{VarDyn} = \frac{\beta_{QP}}{\beta_{rel}} \text{ with } \beta_{QP} = \left| \sum p^{(i)} \right| / \sum E^{(i)}$$

$$\text{and } \beta_{rel} = \frac{2}{M_{frag}(M_{frag} - 1)} \sum_{i < j} |\beta^{(ij)}| \quad \beta^{(ij)} = \beta^{(i)} - \beta^{(j)}. \quad (5)$$

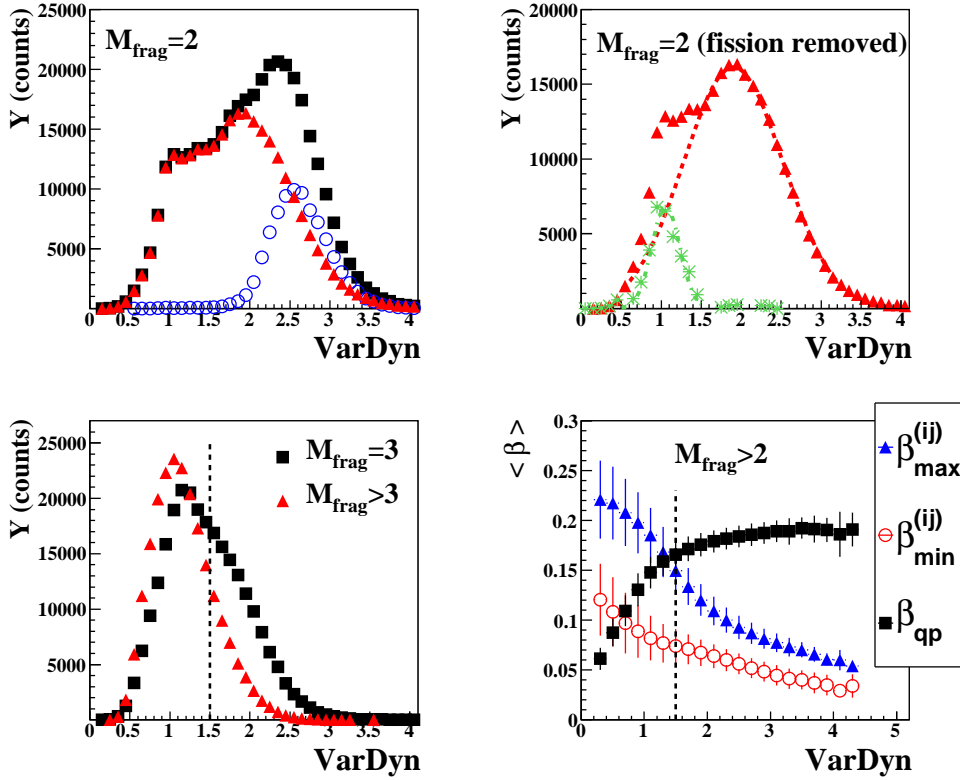


Fig. 2. Top - Left panel: for QP complete events with $M_{frag} = 2$, distribution of VarDyn (eq. 5 - full squares) decomposed into fission events ($Z_1 \times Z_2 \geq 900$ - open circles) and the complementary part (triangles). Right panel: same, with the further decomposition into compact events (dotted line) and non-compact events (stars). Bottom - Left panel: distribution of VarDyn for events with 3 and more than 3 fragments. Right panel: for $M_{frag} > 2$ QP complete events, mean evolution with VarDyn of the minimum and maximum relative velocity between pairs of fragments in an event, and reconstructed QP velocity; error bars indicate the standard deviations of two-dimensional distributions.

$p^{(i)}$, $\beta^{(i)}$ and $E^{(i)}$, which represents the total energy of fragment (i), are defined in the reaction centre of mass. M_{frag} is the number of fragments among the M_{fwd} products. β_{QP} is related to the dissipated energy whereas β_{rel} gives a hint of the dispersion of fragments in velocity space. Compact QP sources should have small values of β_{rel} and thus large values of VarDyn.

With this ratio we compare the average position and distance between fragments with the reconstructed position of the QP in the velocity space to evidence compact configurations corresponding to events with fragments localized around the projectile velocity (larger values of VarDyn). Let us focus first on events with $M_{frag}=2$ (27% of complete events). The distribution of VarDyn is plotted in the left upper part of figure 2: it exhibits a peak for VarDyn=2.4 and a pronounced shoulder for values around 1-1.5. It has long been known that excited Au nuclei will undergo symmetric fission. Fis-

sion of Au QPs was characterized by using the criterion $Z_1 \times Z_2 \geq 900$ [25] (6.3% of complete events). The corresponding distribution of VarDyn (open circles) has a Gaussian shape centered around VarDyn=2.5. Removing the fission contribution, the complementary part still presents a Gaussian shape centered around VarDyn=1.8 with a shoulder for VarDyn<1.5. The right upper part of figure 2 shows the final decomposition with two components (after removing fission): compact QP events (black triangles) and QP events with mid-rapidity fragments (stars), associated with small values of VarDyn. That figure shows that VarDyn>1.5 is a good criterion to select compact QP events with two fragments.

For events with $M_{frag} > 2$, the direct dependence between impact parameter, dissipation, fragment production and velocity of the QPs makes the separation between the two classes of events impossible just starting from the observed VarDyn distributions (see left lower part of figure 2). To test the lower limit previously deduced for $M_{frag}=2$, we introduce the minimum, $\beta_{min}^{(ij)}$, and maximum, $\beta_{max}^{(ij)}$, relative velocity between pairs of fragments calculated for each event. The right lower plot of figure 2 shows the evolution of their mean values $\langle \beta_{min}^{(ij)} \rangle$ and $\langle \beta_{max}^{(ij)} \rangle$ and the evolution of $\langle \beta_{QP} \rangle$ with VarDyn. $\langle \beta_{QP} \rangle$ increases rapidly up to VarDyn around 1.5 and then evolves much more gently, as it is limited by the projectile velocity $\beta_{proj} = 0.2$. For VarDyn values above 1.5, $\langle \beta_{max}^{(ij)} \rangle$ becomes lower than $\langle \beta_{QP} \rangle$, which indicates source velocities sufficiently different from the reaction centre of mass velocity. On the other hand the difference between $\langle \beta_{min}^{(ij)} \rangle$ and $\langle \beta_{max}^{(ij)} \rangle$ remains small above VarDyn around 1.5 whereas it increases for lower VarDyn values. That ensemble of observations confirms that VarDyn=1.5 is a good minimum condition to select compact QP events irrespective of the fragment multiplicity. Let

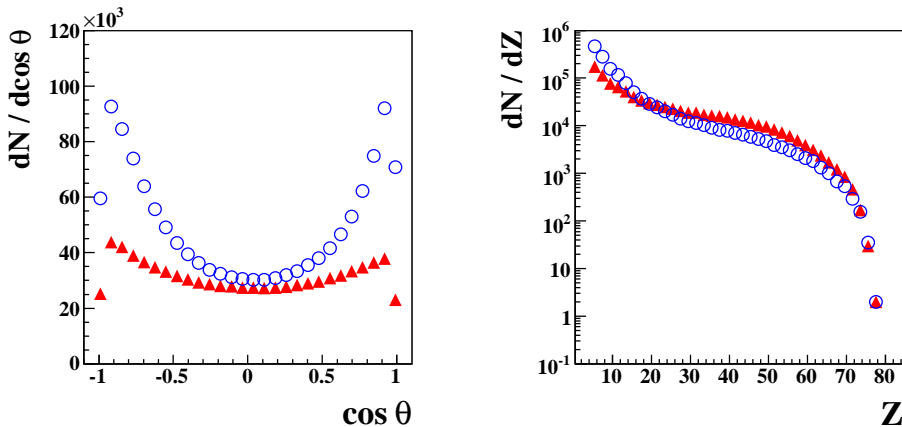


Fig. 3. *Fragment angular (left panel) and charge (right panel) distributions for compact (triangles) and rejected non-compact (open circles) events with $M_{frag} \geq 2$ and fission events removed.*

us come now to a comparison between selected and rejected events. Figure 3

shows, for $M_{frag} \geq 2$ and $Z_1 \times Z_2 < 900$ events, the fragment angular distributions in the QP frame. One notes the much flatter distribution associated with compact events, which indicates a fragment emission closer to isotropy. Information on fragment size distributions is also displayed in the right part of the figure. The rejected events comprise more light fragments ($Z < 20$) than the compact ones.

To summarize, the second and third rows of Table 1 indicate the proportion of the different events at this stage. Compact events, without fission events, correspond to 61.2% of complete events.

	$M_{frag} = 1$	$M_{frag} \geq 2$	Fission	Total
Complete	585885 (39.7%)	797595 (54.0%)	93339 (6.3%)	1476819 (100%)
Compact	585885 (58.8%)	317986 (32.0%)	91840 (9.2%)	995711 (67.4%)
Fission removed	585885 (64.8%)	317986 (35.2%)	-	903871 (61.2%)
Size selection	383730 (81.9%)	84580 (18.1%)	-	468310 (31.7%)

Table 1

Summary of the percentage of different QP events. The second, third and fourth columns refer to events with fragment multiplicities $M_{frag} = 1$, $M_{frag} \geq 2$ and $Z_1 \times Z_2 < 900$ and to fission events ($Z_1 \times Z_2 \geq 900$). At each selection step the last column gives the percentages of kept events relative to the number of complete events.

The light charged particles ($Z < 5$) with positive rapidity in the ellipsoid frame have different origins: mid-rapidity dynamical emissions, pre-equilibrium emissions due to the limited overlap between projectile and target and statistical emissions from QPs and QTs. The evolution of their mean kinetic energy as a function of their emission angle in the QP frame is illustrated in fig. 4 (left panel). The right panel of the figure shows, averaged over all charged particles, the same trend for different excitation energies of QP sources (for the calorimetry procedure - see just after). They clearly show a flatter behaviour for forward angles in the QP source frame. To estimate the contribution of the QP statistical emission we have adopted the method already used in [25] which consists in keeping only the particles emitted forward in the QP frame, and doubling their contribution (charge, mass and energy) assuming a forward-backward symmetric emission.

Note that a large part of the emitted particles (a factor of 3 in multiplicity) are localized in the backward part of the sources. As a consequence, starting from a QP detected charge Z_{fwd} constrained by the completeness criterion, this asymmetry backward/forward leads to large distributions for the sizes of the reconstructed QP sources. To overcome this drawback we have finally selected QP source sizes, Z_s , which correspond to Z_s/Z_{fwd} ratios comprised between 0.9 and 1.0; it is worth noting that the total (rejected) mid-rapidity charge

is on average equal to four for the selected events. This last size selection withholds 31.7% of complete QP events (bottom row of table 1).

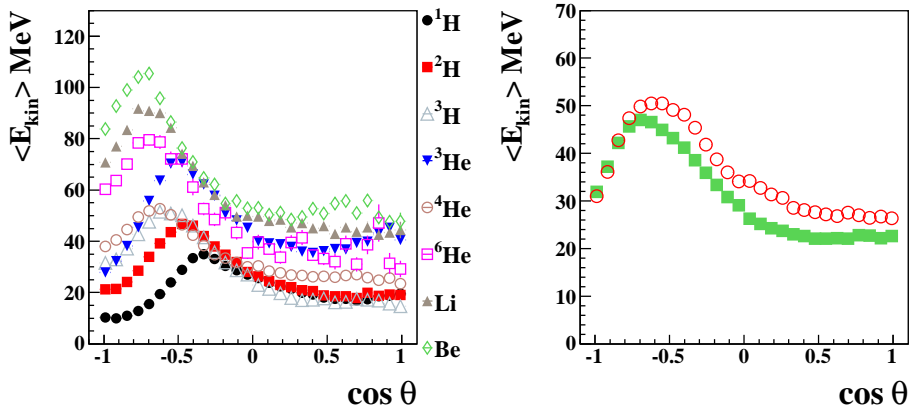


Fig. 4. Left: average kinetic energy vs emission angle in the QP frame of the different light charged particles associated with compact QP sources with $\langle E^* \rangle = 6.3$ AMeV. Right: same but averaged over all charged particles for QP sources with $\langle E^* \rangle = 4.8$ (lower curve) and 7.8 AMeV (upper curve).

The following step consists in the evaluation of the excitation energy of the sources. An event by event calorimetry follows the procedure used above for QF sources. The hypotheses are identical except for charged particle contribution (doubling the forward part) and for fragment masses for which we use the formula ($A=Z(2.045+3.57 \times 10^{-3}Z)$) [21], better adapted for excited nuclei close to the beta stability valley. Note that, compared to the EAL formula, differences for masses appear only for Z greater than 40. The derived excitation energy range for sources was divided in bins of 0.5 AMeV width for comparisons with QF sources.

In the following, we will only use the excitation energy per nucleon as sorting parameter to compare fragment properties from both types of sources. Whereas the relative values of the excitation energies for each type of source should be reliable, one can wonder about the comparison between the excitation energy scales between QF and QP sources. In the next subsection we will present arguments indicating that the two scales are in agreement within 10%.

2.4 Global properties of selected QF and QP sources

The global properties of selected sources are displayed in figure 5. In the left upper part of the figure the evolutions of the source sizes are plotted as a function of their excitation energy per nucleon. The common excitation

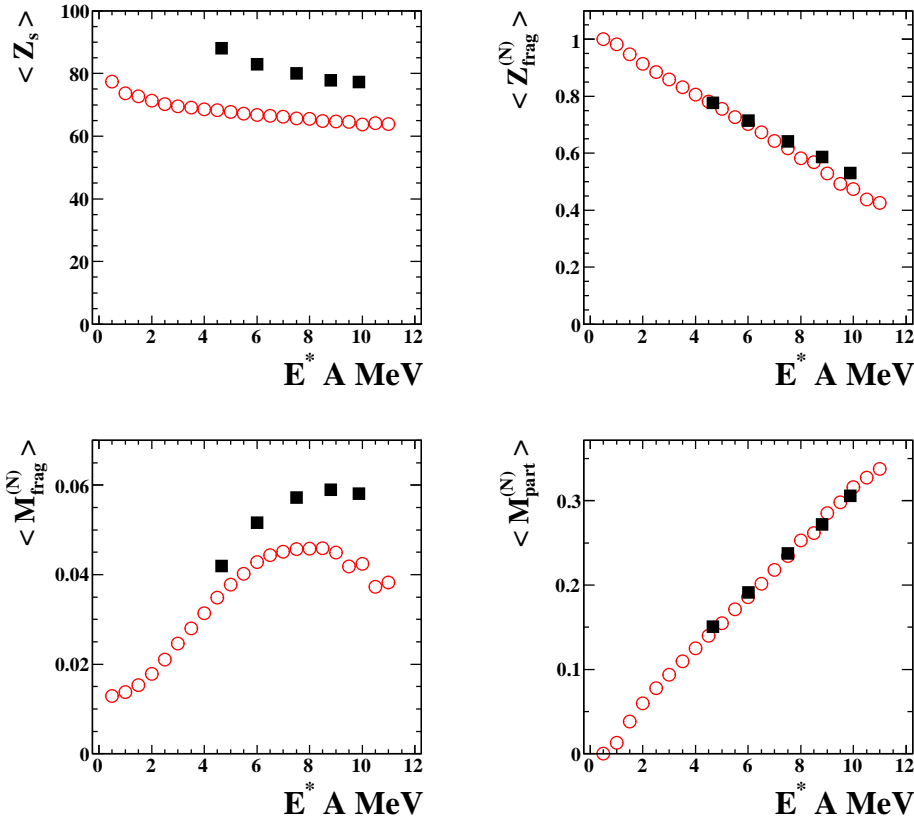


Fig. 5. Full squares and open circles stand respectively for QF and QP sources. Top: average charge of the sources (left) and of the charge bound in fragments normalized to the source charge (right) vs the excitation energy per nucleon. Bottom: average values of the normalized fragment (left) and particle (right) multiplicities.

energy range for the two types of sources is [5,10] AMeV and their variations in charge on that excitation energy range are around ten units of charge; the ratio between the two types of sources is about 1.2-1.3, very close to the Z ratio between Xe+Sn (104) and Au (79). The average proportion of charges bound in fragments as a function of the excitation energy per nucleon is shown in the upper right hand side of figure 5. The quantitative evolution of that observable, normalized to the sizes of the sources, $\langle Z_{frag}^{(N)} \rangle$, is the same for both QF and QP: a linear decrease of charge bound in fragments when the excitation energy per nucleon increases. This behaviour shows that, for a given excitation energy, the sharing among particles and fragments is the same for central and peripheral collisions, which confirms that multifragmentation is mainly driven by the energy deposited into the sources [26]. Thus, the knowledge, for a source, of the proportion of charges bound in fragments (or the complementary knowledge of the total Z found in particles) provides a good estimate of its excitation energy. Note that the proportion varies from about 0.8 to 0.5 in the common excitation energy range. Mean fragment multiplicities normalized to the size of the source are shown in the lower left part of figure 5. Much higher

multiplicities are obtained for QF sources than for QP ones but they both present a maximum in the same excitation energy range (8-10 AMeV). On the other hand the variances of the normalized multiplicity distributions, which are not presented here, are very similar. Finally in the right bottom panel of the figure are displayed the normalized multiplicities of particles $\langle M_{part}^{(N)} \rangle$, which appear completely similar.

3 Fragment charge partitions

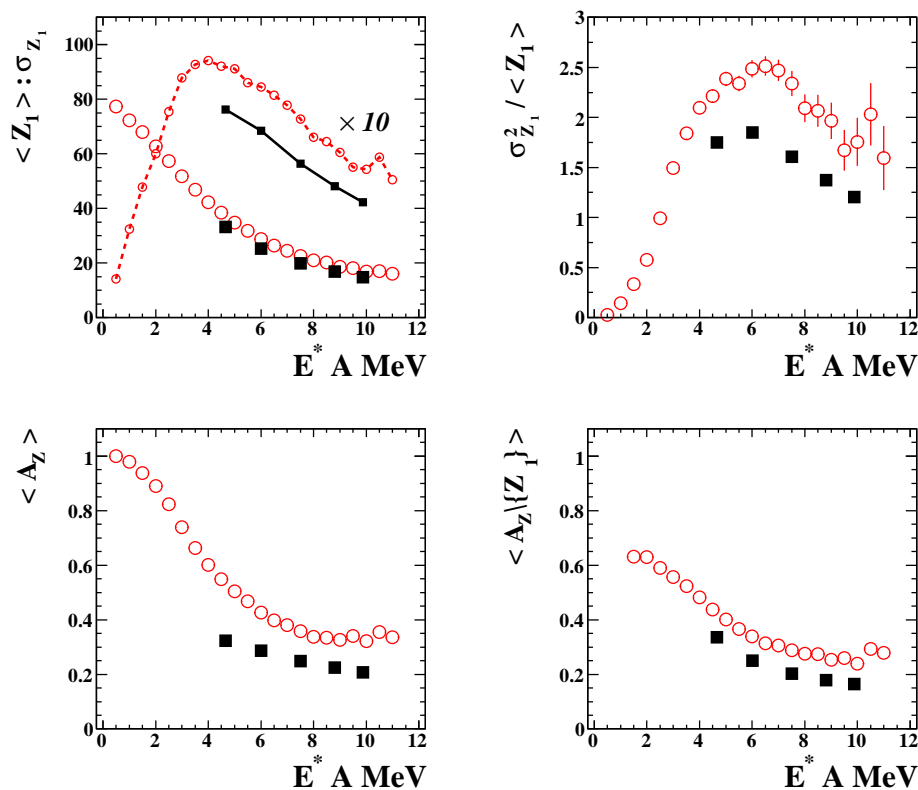


Fig. 6. Full squares and open circles stand respectively for QF and QP sources. Top left: average values and standard deviations (multiplied by 10 - smaller symbols joined by lines) of the charge of the biggest fragment vs the excitation energy per nucleon. Top right: normalized variances of the charge of the biggest fragment vs the excitation energy per nucleon. Bottom: evolution of the charge asymmetry - with (left) and without (right) the biggest fragment - as a function of the excitation energy per nucleon.

As shown previously the percentage of charge bound in fragments is the same for QF and QP sources with the same excitation energy. How is this bound charge shared among fragments? A first answer comes from the properties of the charge of the biggest fragment (Z_1), because several studies point out its specific behaviour [27,28,25] and because it is a good candidate for the order

parameter of a phase transition in hot nuclei [29,30,31,32,33]. In figure 6 (upper left part), the evolutions, with the excitation energy, of its mean value and of the associated fluctuations are plotted. The mean value appears as mainly governed by excitation energy and is largely independent of system sizes and of production modes. This effect was already observed in [34,35] for two QF sources with charges in the ratio 1.5; its occurrence when comparing QF and QP sources would indicate that their excitation energy scales do agree, within 10%. The fluctuations, on the contrary, exhibit sizeable differences. In the common energy range, the standard deviations of Z_1 decrease when the excitation energy increases but they are larger for QP sources. In this latter case they show a maximum value around 4.5 AMeV which is in good agreement with systematics reported for QP sources in [36,37] and seems to correspond to the centre of the coexistence region of phase transition [35,38]. Normalized variances $\sigma_{Z_1}^2 / \langle Z_1 \rangle$ are also reported in figure 6 (upper right part); it was proposed in [39] that the maximum of that observable indicates the critical region of the phase transition. We note that, as compared to standard deviations, normalized variances exhibit a maximum for both QP and QF sources in the excitation energy region 6-7 AMeV, which seems to correspond to the gas-like border of the transition and consequently possibly to the critical region [40,38]. A surprising result coming from that comparison between QP and QF sources is the difference between the behaviours of the charge bound in fragments, Z_{frag} - fig 5 and of Z_1 at a given excitation energy. In the first case one observes a scaling with the size of the sources whereas the second exhibits an independent mean value. How is Z_{frag} partitioned into fragments? An overview of all information related to fragment charge partition can be obtained with a new generalized charge asymmetry variable calculated event by event. For two fragment events ($M_{frag}=2$), the usual proposed observable is $a_{12} = \frac{Z_1-Z_2}{Z_1+Z_2}$ [41]. To take into account distributions of fragment multiplicities which differ for the two sources, the generalized asymmetry (A_Z) reads:

$$A_Z = \frac{1}{\sqrt{M_{frag} - 1}} \frac{\sigma_Z}{\langle Z \rangle} \quad (6)$$

This observable evolves from 1 for asymmetric partitions to 0 for equal size fragment partitions (symmetric). For the one fragment events, mainly present for QP sources, we compute the A_Z observable by taking the first particle in size hierarchy included in calorimetry. In the left bottom part of figure 6, the mean evolution with excitation energy of the generalized asymmetry is shown. Differences are observed which well illustrate how different are the repartitions of Z_{frag} between fragments for QF and QP multifragmenting sources. QP partitions are more asymmetric in the entire common excitation energy range. To be sure that this observation does not simply reflect the peculiar behaviour of the biggest fragment, the generalized asymmetry is re-calculated for partitions

$M_{frag} > 1$, and noted $A_Z \setminus \{Z_1\}$, by removing Z_1 from partitions (bottom right panel of figure 6). The difference between the asymmetry values for the two source types persists. A possible explanation of those experimental results can be found by looking at kinematic properties of fragments [2].

4 Mean fragment relative velocities and radial collective energy.

Radial expansion energy following a compression phase is predicted to be present in semi-classical simulations of central collisions in the Fermi energy domain [42,43,44,45]. In experiments it was obtained, in most of the cases, from comparisons of kinetic properties of fragments with statistical models. For QF sources the centre of mass of the reaction is used as the reference frame to derive kinetic properties of fragments. For QP sources produced in peripheral and semi-peripheral collisions, the definition of the QP frame is correlated to the fragment kinetic energies. Conversely the mean relative velocity between fragments (β_{rel} - eq.5 for $M_{frag} > 1$), is independent of the reference frame, and can provide information about possible radial collective energy.

In the left part of figure 7, the mean evolution of this observable with the excitation energy is plotted for the two types of sources. For QF sources β_{rel} exhibits a linear increase with excitation energy. For QP sources β_{rel} remains almost constant along the E^* range. Fragment velocities are the results of the composition of at most three components: a thermal kinetic part, determined at freeze-out, mainly related to the energy deposit in sources; a Coulomb contribution dependent on the source sizes and an eventual radial extra energy. The effect of the Coulomb contribution can be removed by using a simple normalization (eq.7) which takes into account, event by event, the Coulomb influence in the velocity space of the mean fragment charge ($\langle Z \rangle$) on the complement of the source charge ($Z_s - \langle Z \rangle$).

$$\beta_{rel}^{(N)} = \frac{\beta_{rel}}{\sqrt{\langle Z \rangle (Z_s - \langle Z \rangle)}} \quad (7)$$

The mean behaviour of the $\beta_{rel}^{(N)}$ observable so defined is shown in the right part of figure 7. At an excitation energy of about 5 AMeV, $\beta_{rel}^{(N)}$ values corresponding to QF and QP sources are similar. Above that excitation energy, the values for QF sources exhibit a strong linear increase. For QP sources $\beta_{rel}^{(N)}$ slightly increases up to 9 AMeV excitation energy and saturates above. That saturation can be attributed to the compact source selection. Indeed if one performs the same analysis of QP's (i.e. with the same limit on VarDyn) from Au+Au collisions at 100 AMeV, $\beta_{rel}^{(N)}$ increases faster and saturates at a slightly higher excitation energy, around 10 AMeV (full points in the figure).

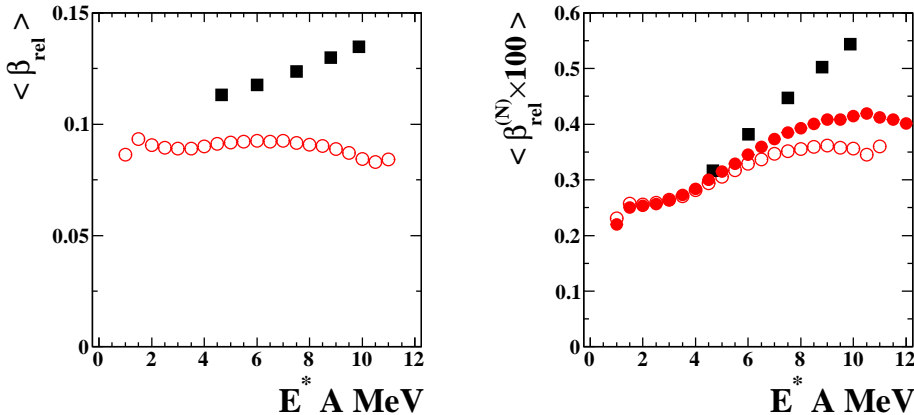


Fig. 7. Full squares and open circles stand respectively for QF and QP sources. Full circles correspond to QP sources produced in 100 A MeV collisions. Evolution of the mean relative velocity of fragments, β_{rel} , (left panel) and of that normalized observable, $\beta_{rel}^{(N)}$, (right panel) with the excitation energy per nucleon.

That fast divergence between the values of $\beta_{rel}^{(N)}$ for the two types of sources signals the well known onset of radial collective expansion for central collisions. Indeed in [40], estimates of radial collective energy (from 0.5 to 2.2 A MeV) for QF sources produced by Xe+Sn collisions are reported for four incident energies: 32, 39, 45 and 50 A MeV. Those estimates were extracted from comparisons with the statistical model SMM assuming a self similar expansion energy. The four estimated values of the radial collective energy (E_R) for the QF sources can be used to calibrate the $\beta_{rel}^{(N)}$ observable. The correspondence between $\beta_{rel}^{(N)}$ and E_R is deduced from a second order polynomial adjustment (dotted line in figure 8). From this function, we extract firstly a radial energy estimate for QF sources formed at 25 A MeV incident energy: 0.1 ± 0.1 A MeV; the error bar being determined from the grey zone in figure 8. In the same way we also deduce two sets (80 and 100 A MeV collisions) of E_R values with their error bars for QP sources using the appropriate mean values of $\beta_{rel}^{(N)}$. For that calibration we take intervals of E^* centered around the mean value, with a width equal to $\pm 3\sigma$, of the corresponding QF source excitation energy distributions. All the quantitative information concerning the evolution of radial energy with excitation energy for both types of sources is presented in figure 9. We have also added the E_R values published by the ISIS collaboration [46] corresponding to the $\pi^- + \text{Au}$ reactions which provide sources equivalent to the QP ones in terms of excitation energy range and size. The observed evolution of E_R for such sources is almost the same as for QP sources. For hadron induced reactions the thermal pressure is the only origin of radial expansion, which indicates that it is the same for QP sources. To be fully convincing, an estimate of the part of the radial collective energy due to thermal pressure calculated with the EES model [47] for an excited nucleus identical to QF sources produced at 50 A MeV incident energy is also reported (open square)

in the figure [48]. To conclude on radial collective energy we have shown that it is essentially produced by thermal pressure in semi-peripheral heavy-ion collisions as it is in hadron induced reactions. For QF sources produced in central heavy-ion collisions the contribution from the compression-expansion cycle becomes more and more important as the incident energy increases.

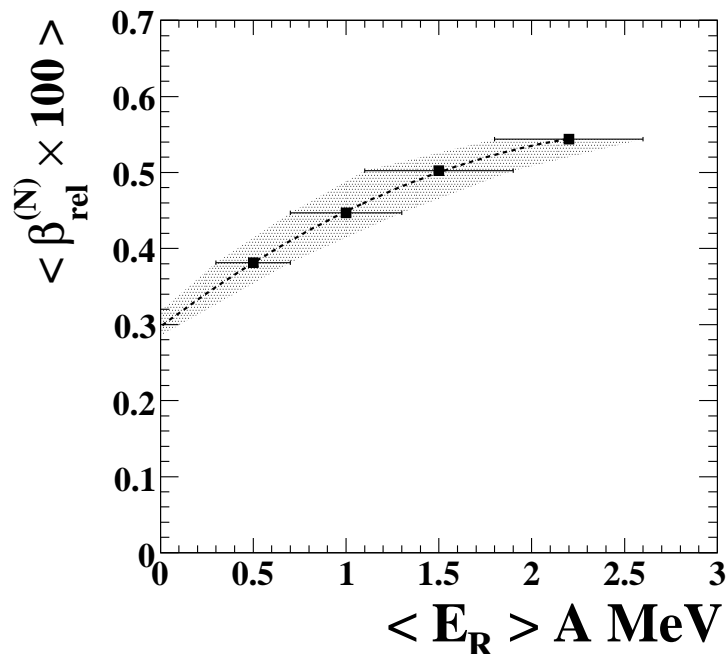


Fig. 8. Radial collective energy calibration. Correspondence between the normalized mean relative velocity of fragments ($\beta_{rel}^{(N)}$) and the radial collective energy E_R ; full squares (Xe+Sn QF sources from 32 to 50 A MeV incident energies) with error bars are used to establish the correspondence (dotted line) between $\beta_{rel}^{(N)}$ and E_R .

5 Discussion and conclusions

We have compared the properties of QF and QP multifragmenting sources in the excitation energy range 5-10 A MeV. They present similarities and differences. Similarities concern: the division of charge among particles and fragments, the particle multiplicities (both normalized to the source size), the average charge of the heaviest fragment of the partitions and the fluctuations of the normalized fragment multiplicities, all the mentioned as a function of excitation energy (including radial collective energy). Differences are first relative to the fluctuations in charge/size of the heaviest fragment, that are larger for QP than for QF sources. That observation was very recently mentioned [37] for normalized quantities $\sigma(Z_1/Z_s)$ and a possible explanation, by comparison

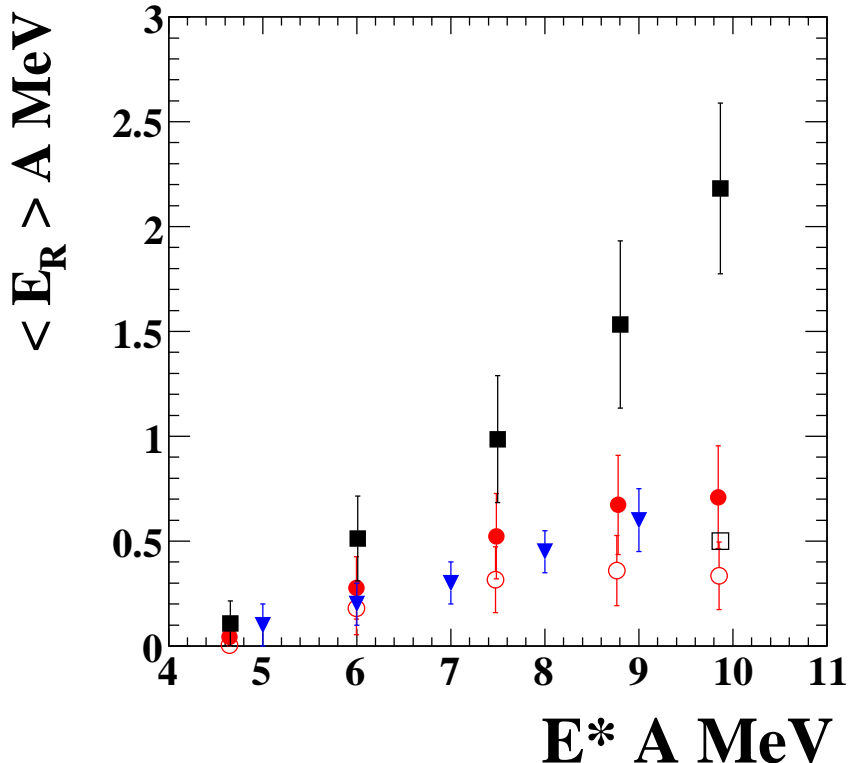


Fig. 9. Radial collective energy. See fig. 7 for symbols for QF and QP sources. Evolution of the radial collective energy with the excitation energy per nucleon for different sources; full triangles correspond to $\pi^- + Au$ reactions [46] and the open square to an estimate of the thermal part of the radial collective energy for Xe+Sn sources produced at 50 A MeV incident energy (see text).

with statistical model (SMM) calculations, was related to different freeze-out volumes. Note that a detailed study using the recently developed theory of universal Δ scaling laws [49,50,25] should also be of the prime interest to make progress on the understanding of the different fluctuations observed. Secondly the asymmetry of the fragment partitions, $A_Z \setminus \{Z_1\}$, is also larger for QP sources; that difference was observed at 5 A MeV excitation energy and above, which corresponds to the onset of collective energy. Thus, the lower asymmetry for QF sources seems to be related to the presence of radial collective expansion coming from the compression-expansion cycle for central collisions. Finally normalized fragment multiplicities for QF sources are also significantly larger above 5 A MeV. Clearly the degree of fragmentation of the system increases with the radial collective energy and partitions are also affected. What is the influence of the radial collective energy on the region where QF and QT sources break in the phase diagram (plane freeze-out volume - excitation energy)?

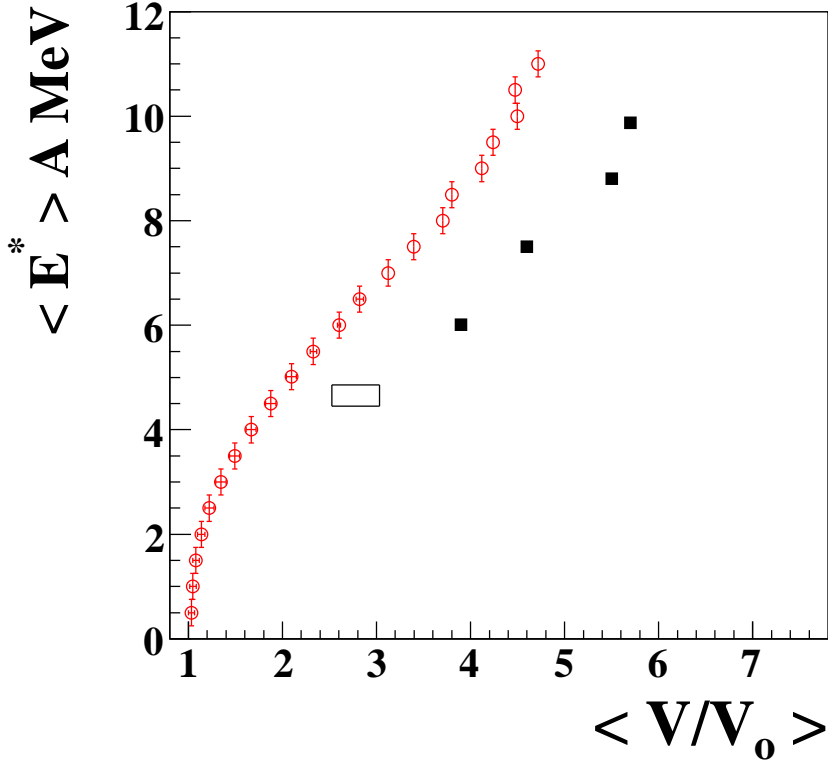


Fig. 10. Fragmentation position in the excitation energy-freeze-out volume plane. The four full squares are taken from [51]. The open rectangle gives the estimated position (with error bar) for QF source at 25 AMeV, and the open circles those for QP sources.

Estimates of freeze-out volumes for QF sources produced in Xe+Sn collisions for incident energies between 32 and 50 AMeV were very recently obtained (details can be found in [51]). They evolve from 3.9 to 5.7 V/V_0 , where V_0 would correspond to the volume of the source at normal density. These results were extracted from simulations using experimental data and agree rather well with those deduced from the statistical model MMM [52,53]. In a first attempt to calibrate the freeze-out volumes for other sources, we use the charge of the heaviest fragment $\langle Z_1^{(N)} \rangle$ or the fragment multiplicity $\langle M_{frag}^{(N)} \rangle$, normalized to the size of the source, as representative of the volume or density at break-up. From the four points for QF sources and the additional constraint that $Z_1^{(N)} = M_{frag} = 1$ at $V/V_0 = 1$, we obtain two relations $V/V_0 = f_1(Z_1^{(N)})$ and $V/V_0 = f_2(M_{frag}^{(N)})$, from which we calculate the volumes for QF sources at 25 AMeV and for QP sources. The results are plotted in fig. 10, with error bars coming from the difference between the two estimates using f_1 and f_2 ; note that error bars for the QP volumes are small up to 7 AMeV, and can not be estimated above, due to the fall of $\langle M_{frag}^{(N)} \rangle$ at high energy (see fig. 5).

The volumes of QP sources are smaller than those of QF sources (about $1.2 \times V/V_0$ for $E^*=10$ AMeV). This supports the observation made previously starting from fluctuations of the charge of the heaviest fragment in a partition (see figures 13 and 18 in [37]). It is worth noting that a freeze-out volume significantly larger than that of a QP source ($2.75 \pm 0.25 V/V_0$ compared to $1.9 V/V_0$) at the same excitation energy per nucleon is found for QF sources at 25 AMeV. This could indicate that as soon as compression-expansion occurs, larger volumes are involved.

To conclude, we have compared in detail the static properties of hot fragmenting sources produced in central (QF) and semi-peripheral (QP) collisions. From kinematical properties of fragments, information on the different radial collective energies involved was deduced using mean fragment relative velocities, a comparison with hadron-nucleus results and an estimate of the part of the radial collective energy due to thermal pressure. The major results are the following. The weak radial collective energy observed for QP sources is shown to originate from thermal pressure only; it reaches about 0.7 AMeV at an excitation energy of 10 AMeV. The larger fragment multiplicities observed for QF sources and their more symmetric fragmentation must be related to the extra radial collective energy produced by the compression-expansion cycle occurring in central collisions. Such a cycle seems to lead fused systems to break at lower density.

Appendix

The values reported in this paper for the excitation energies of the hot sources sometimes differ from those published by the INDRA collaboration for the same systems. In this appendix we will examine the influence of the parameters entering the calorimetric equation on the excitation energy per nucleon of the sources.

The excitation energy, E^* , of a hot source is calculated event by event with the relation

$$E_s^* = \sum_{M_{cp}} E_{cp} + \sum_{M_n} E_n - Q. \quad (8)$$

M_{cp} , E_{cp} and M_n , E_n are respectively the multiplicities and kinetic energies of charged products and neutrons belonging to the source; Q is the mass difference between the source and all final products. Energies are expressed in the source reference frame.

We consider Xe+Sn QF sources, for which the reference frame is the well

defined reaction centre of mass, and discuss only the average values (we know that the procedure used for calorimetry broadens the distributions). We have firstly verified that the definition of a fragment ($Z \geq 3$ or $Z \geq 5$) has no influence (less than 0.05 AMeV) on the excitation energy of the source.

As for all results obtained with the INDRA array, neutrons are not detected. Their multiplicity is equal to the difference between the mass of the source and the sum of those of the final products. The source is assumed to have the same N/Z ratio as the initial system (projectile + target). The fragment masses are derived in the present paper from the EAL estimate. In other papers, the mass of the β -stability valley is chosen [37]. These two mass formulae differ for large fragments $Z > 20$. However due to rounding up compensations for the light fragment masses, it appears that, when using the β -stability mass, the neutron number is 2 units (7%) larger at 32 AMeV and 5 units (20%) larger at 50 AMeV. The Q-value also depends on the neutron multiplicity, at the level of a few percents.

The kinetic energy of neutrons is calculated by firstly assuming that the source has a temperature T given by: $E_s^* = (A_s/k)T^2$, which, introduced in the former equation gives:

$$E_s^* = \sum_{M_{cp}} E_{cp} + M_n f T - Q. \quad (9)$$

If the neutrons are all emitted at freeze-out, the factor f is equal to 1.5, whereas it is equal to 1 if all neutrons are evaporated along a long chain [54]. Obviously, the final calculated excitation energy will be higher when f is larger. The level density parameter plays also a role in the determination of E^* , the value of which slightly increasing with k .

Finally we give in the following table the values of the different terms of eq. 9 with the two sets of hypotheses used in the present paper (second and fourth rows) and in ref. [37] (third and fifth rows).

If we use all sets of data obtained by varying the fragment mass (EAL, β -stability), the factor f (1.0 and 1.5) and the level density parameter ($k=8,10$), we end-up with values of the excitation energies per nucleon which differ at most by 1.2 MeV at 50 AMeV and 0.8 MeV at 32 AMeV. This helps putting systematic error bars on the excitation energy, $\pm 6.5\%$ at 32 AMeV and $\pm 6\%$ at 50 AMeV. These systematic error bars are in agreement with the estimates of [55,56]. Note that the relative values of E^*/A at the different bombarding energies are little modified.

E_{inc}	Z_{frag}^{min}	A_f	k	f	$\sum E_{cp}$	Q	T	M_n	E^*
50	5	EAL	10	1.0	6.10	2.34	9.92	26.6	9.88
50	3	β	8	1.5	6.24	2.46	9.38	31.9	11.04
32	5	EAL	10	1.0	3.62	1.39	7.73	26	6.01
32	3	β	8	1.5	3.72	1.40	7.27	27.9	6.64

Table 2

Calorimetry results for central Xe+Sn reactions with two different sets of hypotheses. The left part lists the hypotheses, Z_{frag}^{min} is the minimum fragment charge. The right part gives the results. All values are in MeV per nucleon, except T (in MeV). The events considered have a total detected charge equal to at least 80% of the system charge.

References

- [1] WCI proceedings, P. Chomaz et al. (eds.) Dynamics and Thermodynamics with nuclear degrees of freedom, Springer, 2006, vol. 30 of *Eur. Phys. J. A*, 1–342.
- [2] G. J. Kunde et al., *Phys. Rev. Lett.* 74 (1995) 38.
- [3] J. B. Natowitz et al., *Phys. Rev. C* 66 (2002) 031601.
- [4] M. D’Agostino et al., *Nucl. Phys.* 724 (2003) 455.
- [5] Y. G. Ma et al., *Phys. Rev. C* 71 (2005) 054606.
- [6] B. Borderie, *J. Phys. G: Nucl. Part. Phys.* 28 (2002) R217.
- [7] C. P. Montoya et al., *Phys. Rev. Lett.* 73 (1994) 3070.
- [8] J. F. Dempsey et al., *Phys. Rev. C* 54 (1996) 1710.
- [9] E. Plagnol et al. (INDRA Collaboration), *Phys. Rev. C* 61 (1999) 014606.
- [10] J. Lukasik et al. (INDRA and ALADIN collaborations), *Phys. Lett. B* 566 (2003) 76.
- [11] J. Pouthas et al., *Nucl. Instr. and Meth. in Phys. Res. A* 357 (1995) 418.
- [12] J. Pouthas et al., *Nucl. Instr. and Meth. in Phys. Res. A* 369 (1996) 222.
- [13] G. Tăbăcaru et al. (INDRA Collaboration), *Nucl. Instr. and Meth. in Phys. Res. A* 428 (1999) 379.
- [14] M. Pârlog et al. (INDRA Collaboration), *Nucl. Instr. and Meth. in Phys. Res. A* 482 (2002) 693.
- [15] M. Pârlog et al. (INDRA Collaboration), *Nucl. Instr. and Meth. in Phys. Res. A* 482 (2002) 674.
- [16] A. Trzciński et al. (INDRA and ALADIN collaborations), *Nucl. Inst. Meth. A* 501 (2003) 367.

- [17] J. F. Lecomte et al., *Phys. Lett. B* 325 (1994) 317.
- [18] J. D. Frankland et al. (INDRA Collaboration), *Nucl. Phys. A* 689 (2001) 905.
- [19] J. D. Frankland et al. (INDRA Collaboration), *Nucl. Phys. A* 689 (2001) 940.
- [20] V. E. Viola et al., P. Chomaz et al. (eds.) *Dynamics and Thermodynamics with nuclear degrees of freedom*, Springer, 2006, vol. 30 of *Eur. Phys. J. A*, 215–226.
- [21] R. J. Charity, *Phys. Rev. C* 58 (1998) 1073.
- [22] T. Lefort et al. (INDRA Collaboration), *Nucl. Phys. A* 662 (2000) 397.
- [23] J. Colin et al. (INDRA Collaboration), *Phys. Rev. C* 67 (2003) 064603.
- [24] S. Piantelli et al., *Phys. Rev. C* 74 (2006) 034609.
- [25] M. Pichon et al. (INDRA and ALADIN collaborations), *Nucl. Phys. A* 779 (2006) 267.
- [26] B. Tamain, P. Chomaz et al. (eds.) *Dynamics and Thermodynamics with nuclear degrees of freedom*, Springer, 2006, vol. 30 of *Eur. Phys. J. A*, 71–79.
- [27] P. Désesquelles et al. (Multics/Miniball Collaboration), *Nucl. Phys. A* 633 (1998) 547.
- [28] G. Tăbăcaru et al. (INDRA Collaboration), *Nucl. Phys. A* 764 (2006) 371.
- [29] A. Bonasera et al., *Rivista Nuovo Cimento* 23 (2000) 1.
- [30] J. M. Carmona et al., *Phys. Lett. B* 531 (2002) 71.
- [31] J. D. Frankland et al. (INDRA and ALADIN collaborations), *Nucl. Phys. A* 749 (2005) 102.
- [32] F. Gulminelli et al., *Phys. Rev. C* 71 (2005) 054607.
- [33] G. Chaudhuri et al., *Phys. Rev. C* 75 (2007) 034603.
- [34] M. F. Rivet et al. (INDRA Collaboration), *Phys. Lett. B* 430 (1998) 217.
- [35] E. Bonnet, thèse de doctorat, Université Paris-XI Orsay (2006), <http://tel.archives-ouvertes.fr/tel-00121736>.
- [36] F. Gulminelli et al., P. Chomaz et al. (eds.) *Dynamics and Thermodynamics with nuclear degrees of freedom*, Springer, 2006, vol. 30 of *Eur. Phys. J. A*, 253–262.
- [37] N. Le Neindre et al. (INDRA and ALADIN collaborations), *Nucl. Phys. A* 795 (2007) 47.
- [38] E. Bonnet et al. (INDRA and ALADIN collaborations), submitted to *Phys. Rev. Lett.*
- [39] C. O. Dorso et al., *Phys. Rev. C* 60 (1999) 034606.

- [40] B. Borderie et al., Nucl. Phys. A 734 (2004) 495.
- [41] P. Kreutz et al., Nucl. Phys. A 556 (1993) 672.
- [42] J. J. Molitoris et al., Phys. Rev. C 37 (1988) 1020.
- [43] G. F. Bertsch et al., Phys. Rep. 160 (1988) 189.
- [44] E. Suraud et al., Phys. Lett. B 229 (1989) 359.
- [45] A. Bonasera et al., Phys. Rep. 243 (1994) 1.
- [46] L. Beaulieu et al., Phys. Rev. C 64 (2001) 064604.
- [47] W. A. Friedman, Phys. Rev. C 42 (1990) 667.
- [48] B. Borderie, G. Giardina et al. (eds.) Proc. Int. Symposium on large-scale collective motions of atomic nuclei, Brolo, Italy, World scientific, 1997, 1.
- [49] R. Botet et al., Phys. Rev. Lett. 86 (2001) 3514.
- [50] J. D. Frankland et al. (INDRA and ALADIN collaborations), Phys. Rev. C 71 (2005) 034607.
- [51] S. Piantelli et al. (INDRA Collaboration), Nucl. Phys. A 809 (2008) 111.
- [52] A. H. Raduta et al., Phys. Rev. C 55 (1997) 1344.
- [53] A. H. Raduta et al., Phys. Rev. C 61 (2000) 034611.
- [54] M. Gonin et al., Phys. Lett. B 217 (1989) 406.
- [55] M. D'Agostino et al., Nucl. Phys. A 699 (2002) 795.
- [56] E. Vient, Habilitation à diriger des recherches, Université de Caen (2006), <http://tel.archives-ouvertes.fr/tel-00141924>.